

## Statistical analyses on the energies of X-ray plateaus and flares in gamma-ray bursts

SHUANG-XI YI,<sup>1</sup> MEI DU,<sup>1</sup> AND TONG LIU<sup>2</sup>

<sup>1</sup>*School of Physics and Physical Engineering, Qufu Normal University, Qufu, Shandong 273165, China*

<sup>2</sup>*Department of Astronomy, Xiamen University, Xiamen, Fujian 361005, China*

(Received; Revised; Accepted)

Submitted to ApJ

### ABSTRACT

Distinct X-ray plateau and flare phases have been observed in the afterglows of gamma-ray bursts (GRBs), and most of them should be related to central engine activities. In this paper, we collect 174 GRBs with X-ray plateau phases and 106 GRBs with X-ray flares. There are 51 GRBs that overlap in the two selected samples. We analyze the distributions of the proportions of the plateau energy  $E_{\text{plateau}}$  and the flare energy  $E_{\text{flare}}$  relative to the isotropic prompt emission energy  $E_{\gamma,\text{iso}}$ . The results indicate that they well meet the Gaussian distributions and the medians of the logarithmic ratios are  $\sim -0.96$  and  $-1.39$  in the two cases. Moreover, strong positive correlations between  $E_{\text{plateau}}$  (or  $E_{\text{flare}}$ ) and  $E_{\gamma,\text{iso}}$  with slopes of  $\sim 0.95$  (or  $\sim 0.80$ ) are presented. For the overlapping sample, the slope is  $\sim 0.80$ . We argue that most of X-ray plateaus and flares might have the same physical origin but appear with different features because of the different circumstances and radiation mechanisms. We also test the applicabilities of two models, i.e., black holes surrounded by fractured hyperaccretion disks and millisecond magnetars, on the origins of X-ray plateaus and flares.

*Keywords:* accretion, accretion disks - black hole physics - gamma-ray burst: general - stars: magnetar

### 1. INTRODUCTION

Gamma-ray bursts (GRBs) are the most powerful explosions in the universe. According to their duration, GRBs are divided into two groups: long-duration GRBs (LGRBs,  $T_{90} > 2$  s) and short-duration GRBs (SGRBs,  $T_{90} < 2$  s). It is widely believed that they originate from massive collapsars (e.g., Woosley 1993; MacFadyen & Woosley 1999) and binary compact object mergers (e.g., Paczyński 1986; Eichler et al. 1989; Narayan et al. 1992). Currently, GRB central engines are still uncertain, but there are two leading models, i.e., the stellar-mass black hole (BH) hyperaccretion model (e.g., Woosley 1993; Popham et al. 1999; Narayan et al. 2001; Yi et al. 2017; Liu et al. 2018, 2019) and for a review see Liu et al. (2017) and the model of a rapidly rotating neutron star (NS) with a strong magnetic field of  $\sim 10^{15}$  G,

namely, a millisecond magnetar (e.g., Usov 1992; Dai & Lu 1998a,b; Zhang & Mészáros 2001).

Since Neil Gehrels *Swift* satellite was successfully launched in 2004 (Gehrels et al. 2004), both LGRBs and SGRBs with remarkable X-ray plateaus and flares have been observed. It is widely believed that the X-ray plateaus and flares might be linked to the central engine activity, which are different from the X-ray afterglows originating from the fireball shell decelerated in the circumburst medium (e.g., Rees & Mészáros 1992; Mészáros & Rees 1997; Panaitescu et al. 1998; Sari et al. 1998; Zou et al. 2005; Fan & Piran 2006; Yi et al. 2013, 2020; Zhou et al. 2020). Approximately half of *Swift* GRBs show remarkable plateaus or flares in their X-ray afterglows (e.g., Yi et al. 2016; Tang et al. 2019). X-ray plateaus usually appear in the early afterglow phase with a flat segment, and two different kinds of decay are followed, which are named “internal” and “ordinary” plateaus with power-law decay indices of  $< -3$  and  $> -3$ , respectively (see e.g., Nousek et al. 2006; Zhang et al. 2006; O’Brien & Willingale 2007; Sakamoto

et al. 2007; Dainotti et al. 2008, 2010, 2011a, 2013a, 2016; Du 2020) and for a review see Dainotti & Del Vecchio (2017). A similar shallow decay also occurs in the optical light curves (e.g., Si et al. 2018; Dainotti et al. 2020) and *Fermi*-LAT GRBs (e.g., Dainotti et al. 2021). The typical timescales of the X-ray plateaus in LGRBs and SGRBs are approximately several hundred and several thousand seconds, respectively. Generally, the extra energy injections from the spin-down of a millisecond magnetar (e.g., Dai & Lu 1998a,b; Zhang & Mészáros 2001; Rowlinson et al. 2010; Bucciantini et al. 2012; Gompertz et al. 2013; Du 2020) or a supramassive fast-rotating quark star (e.g., Li et al. 2016; Hou et al. 2018; Ouyed et al. 2020) are expected to explain the plateaus. Other models on the jet modes, such as the two-component ejecta (e.g., Toma et al. 2006; Yamazaki 2009), jets with microphysical factor evolutions (e.g., Ioka et al. 2006; Panaitescu et al. 2006) or bulk Lorentz factor distributions (e.g., Uhm & Beloborodov 2007), delayed deceleration jets (e.g., Duffell & MacFadyen 2015), and off-axis jets (e.g., Beniamini et al. 2020), have been proposed. Moreover, Huang & Liu (2021) proposed that regardless of the type of central engine, the energy injection driven by the long-lasting precessing jets can also produce plateau phases.

The shapes of X-ray flares generally exhibit a rapid rise and a slow decay (e.g., Burrows et al. 2005; Falcone et al. 2007; Chincarini et al. 2010). Because of the different temporal behaviors and spectral properties of the afterglows, they are thought to have the same physical origin as the prompt emission of GRBs, and parts of them are triggered by the long-lasting activities or restart of the central engines (e.g., Margutti et al. 2010, 2011; Mu et al. 2016, 2018). Some theoretical models of X-ray flares have been provided, such as accretion of the fragmentation from a rapidly rotating collapsar (King et al. 2005), differential rotation in a post-merger millisecond magnetar (e.g., Dai et al. 2006), a magnetic switch of the accretion process (Proga & Zhang 2006), fragmentation of an accretion disk (e.g., Perna et al. 2006), transition of the accretion modes (Lazzati et al. 2008), radial or vertical outflows caused by the instabilities of a BH hyperaccretion disk (Liu et al. 2008, 2014), He-synthesis-driven disk winds (Lee et al. 2009), precessing jets (e.g., Liu et al. 2010; Hou et al. 2014), dynamical instability in jets (Lazzati et al. 2011), episodic jets produced by the magnetohydrodynamic process in an accretion disk (Yuan & Zhang 2012), and magnetic coupling in a BH hyperaccretion disk (Luo et al. 2013).

The characteristics of X-ray plateaus and flares might indicate that the central engines were always active in the whole explosions. In other words, the duration of

central engine activity should be much longer than the observed timescale of GRB prompt emission itself (e.g., Zhang et al. 2014; Liu et al. 2018). However, it is also difficult to determine exactly which type of central engine powers these peculiar variabilities.

In this paper, we collect two samples of GRBs with X-ray plateau and flare activity features and obtain isotropic prompt emission energies  $E_{\gamma,\text{iso}}$ , X-ray plateau energies  $E_{\text{plateau}}$ , and isotropic X-ray flare energies  $E_{\text{flare}}$ . Then, we analyze the distributions of the energy proportions and some correlations between  $E_{\text{plateau}}$  (or  $E_{\text{flare}}$ ) and  $E_{\gamma,\text{iso}}$ , which might provide clues and evidence on their physical mechanisms. This paper is organized as follows. The sample selection and data reduction processes are described in Section 2. In Section 3, we analyze the energy correlations. Two possible models are tested in Section 4, and a brief summary is provided in Section 5.

## 2. DATA

The observations of *Swift* GRBs promote our knowledge on the taxonomy and morphology of GRBs, especially the many X-ray plateaus and flares detected in afterglows (e.g., Zhang et al. 2006; Nousek et al. 2006). We collected GRBs with plateau and flare features in X-ray afterglows and divided them into two groups. The plateau sample is adopted from Tang et al. (2019), which includes 174 GRBs observed from May 2005 to August 2018. The screening criteria are extremely strict, and three criteria are applied, i.e., (1) a smoothly broken power-law function is usually used to fit the afterglows with plateaus, and then the power-law index of the plateaus in the range of  $\sim -1.0$  to  $1.0$  is selected; (2) rich data points are required; and (3) the GRB redshift should be given. More details on the data selection can be found in Tang et al. (2019). In this work, we choose the following GRB parameters: the redshift  $z$ , the isotropic energy of prompt emission  $E_{\gamma,\text{iso}}$ , and the isotropic plateau energy  $E_{\text{plateau}}$ , which are shown in Table 1. The plateau phase energy is given by  $E_{\text{plateau}} = T_{\text{a}}L_X(1+z)$ , where  $T_{\text{a}}$  is the end time of the plateau phase in the GRB rest frame and  $L_X$  is the X-ray luminosity at the end time. This correlation was already previously discovered in Dainotti et al. (2008, 2010, 2013b, 2015a, 2017). Most GRBs with plateaus belong to LGRBs, and only a small fraction are classified as SGRBs, including GRBs 051221A, 061201, 070809, 090510, 130603B, 140903A, and 150423A.

Furthermore, 106 GRBs with X-ray flares are collected. Most of them are taken from Yi et al. (2016), and the others are adopted from Falcone et al. (2007), Chincarini et al. (2010), Bernardini et al. (2011), and

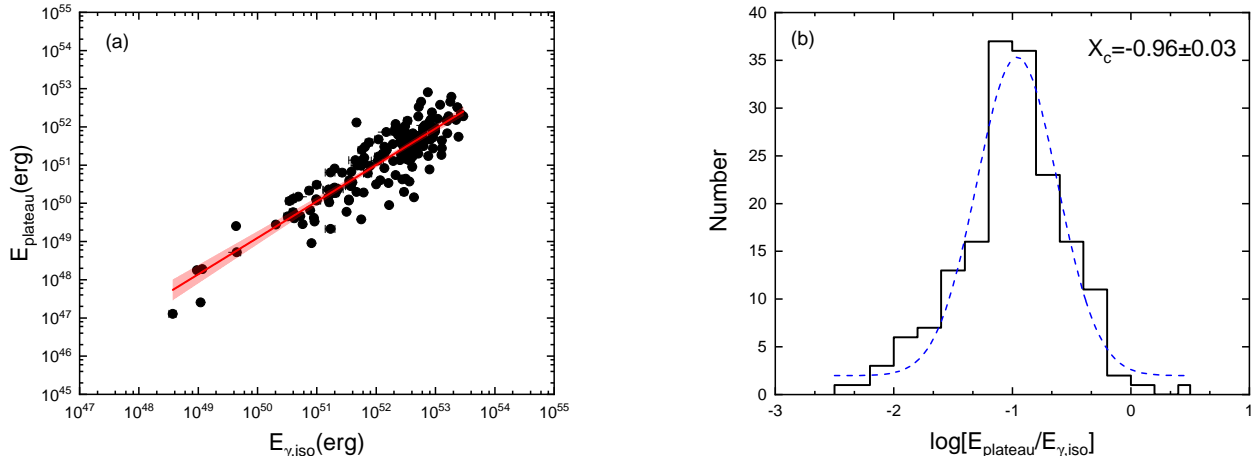


**Figure 1.** *Panel (a):* Correlation of  $E_{\text{plateau}} - E_{\gamma,\text{iso}}$ . The red solid line denotes the linear fitting with the slope  $\sim 0.95 \pm 0.04$ , and the light red region represents a 95% confidence interval. *Panel (b):* Histogram of  $\log(E_{\text{plateau}}/E_{\gamma,\text{iso}})$ . The blue dashed line denotes the Gaussian fitting with  $X_c = -0.96 \pm 0.03$ .

Yi et al. (2015). The selected GRBs with X-ray flares are all LGRBs. For GRBs with two or more flares, the sum of these flare energies is considered as the flare energy  $E_{\text{flare}}$ , which can be obtained by  $E_{\text{flare}} = 4\pi D_L^2 S_F / (1+z)$ , where  $D_L$  and  $S_F$  are the luminosity distance and the fluence of X-ray flares, respectively. Meanwhile, the corresponding  $E_{\gamma,\text{iso}}$  can be obtained from Li Y et al. (2016), Ruffini et al. (2018), Wang et al. (2018), Tang et al. (2019), Fana Dirirsa et al. (2019), Minaev & Pozanenko (2020), Hao et al. (2020), and Du et al. (2021). The X-ray flare data, including the redshift  $z$ , the isotropic energy of prompt emission  $E_{\gamma,\text{iso}}$ , and the total flare energy  $E_{\text{flare}}$ , are listed in Table 2.

Interestingly, 51 GRBs overlapped in the two samples, which means that both plateaus and flares appeared in their X-ray afterglows. The overlapping data are labeled in boldface in Tables 1 and 2.

### 3. STATISTICAL ANALYSES

Since most X-ray plateaus and flares are closely related to the activities of the GRB central engines, we speculate that they might have similar statistical properties. Then, we study these possibilities by analyzing the statistical relations between  $E_{\text{plateau}}$  (or  $E_{\text{flare}}$ ) and  $E_{\gamma,\text{iso}}$ , as well as the ratio of  $E_{\text{plateau}}$  (or  $E_{\text{flare}}$ ) to  $E_{\gamma,\text{iso}}$ . The first time  $E_{\gamma,\text{iso}}$  v.s.  $L_X$  was proposed by Dainotti et al. (2011b), later updated in Dainotti et al. (2015b). Also  $E_{\gamma,\text{iso}}$  v.s.  $T_a$  has been investigated, where  $L_X - T_a$  are anti-correlated (Dainotti et al. 2008).

Figures 1(a) and 1(b) show the correlation between  $E_{\text{plateau}}$  and  $E_{\gamma,\text{iso}}$  and the distributions of  $\log(E_{\text{plateau}}/E_{\gamma,\text{iso}})$ , respectively. Obviously, the posi-

tive correlation with a slope of  $\sim 0.95 \pm 0.04$  is very strong, and the median of the Gaussian distribution on  $\log(E_{\text{plateau}}/E_{\gamma,\text{iso}})$  is approximately  $-0.96 \pm 0.03$ , i.e., the typical plateau energy  $E_{\text{plateau}}$  is approximately a tenth of the typical energy of prompt emission  $E_{\gamma,\text{iso}}$ .

Figures 2(a) and 2(b) display a similar correlation and contribution but for the isotropic flare energy  $E_{\text{flare}}$ . The positive correlation between  $E_{\text{flare}}$  and  $E_{\gamma,\text{iso}}$  with a slope of  $\sim 0.80 \pm 0.09$  is slightly looser than the correlation in Figure 1(a). We consider that this issue might be resulted in some of X-ray flares related to the external origins (e.g., Margutti et al. 2010, 2011; Mu et al. 2016). The median of the Gaussian distribution on  $\log(E_{\text{flare}}/E_{\gamma,\text{iso}})$  is approximately  $-1.39 \pm 0.03$ . Interestingly, the behaviors of the above correlation and distribution on the plateaus are similar to those on the flares.

In addition, Figure 3 shows the correlations and distributions of 51 GRBs with both X-ray plateaus and flares. The correlations of  $E_{\text{plateau}} - E_{\gamma,\text{iso}}$ ,  $E_{\text{flare}} - E_{\gamma,\text{iso}}$ , and  $(E_{\text{plateau}} + E_{\text{flare}}) - E_{\gamma,\text{iso}}$  for 51 GRBs have almost the same tendency with slopes of  $\sim 0.85 \pm 0.09$ ,  $0.76 \pm 0.14$ , and  $0.82 \pm 0.08$ , respectively. The Gaussian distributions for  $\log(E_{\text{plateau}}/E_{\gamma,\text{iso}})$  and  $\log(E_{\text{flare}}/E_{\gamma,\text{iso}})$  of the overlapping GRBs show similar Gaussian distributions, and the central values are approximately  $-1.10 \pm 0.06$  and  $-0.98 \pm 0.05$ , respectively. As shown in Figure 3(f), the distribution of  $\log[(E_{\text{plateau}} + E_{\text{flare}})/E_{\gamma,\text{iso}}]$  shows a bimodal distribution, which is caused by the amplifying dispersions once the values of  $E_{\text{plateau}}$  and  $E_{\text{flare}}$  mixed together, but the correlation of  $(E_{\text{plateau}} + E_{\text{flare}}) - E_{\gamma,\text{iso}}$  still seems tight with a slope of  $\sim 0.82 \pm 0.08$ . All of the

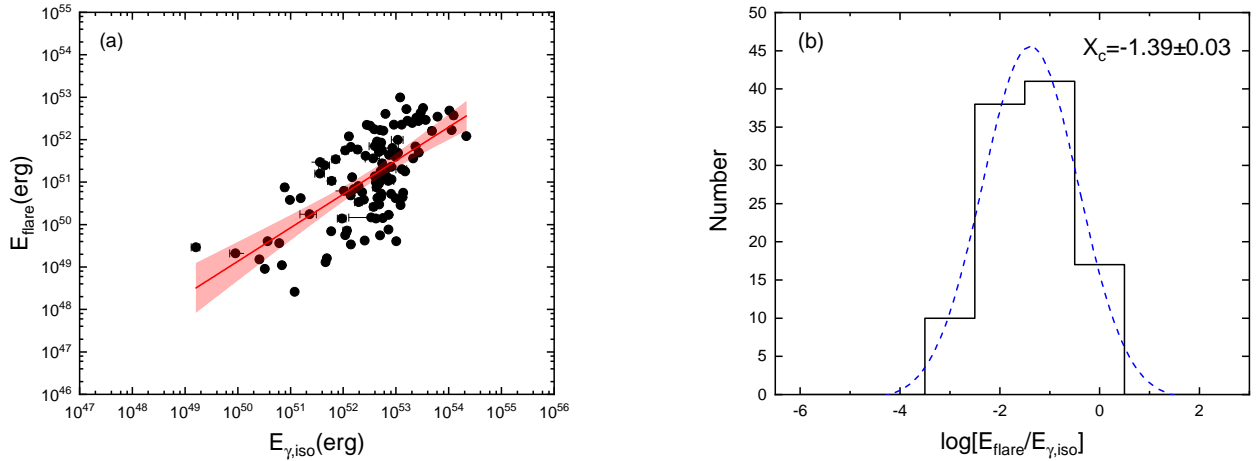


**Figure 2.** *Panel (a):* Similar to Figure 1(a) but for X-ray flares with a slope of  $\sim 0.80 \pm 0.09$ . *Panel (b):* Similar to Figure 1(b) but  $X_c = -1.37 \pm 0.02$ .

best linear fitting results in the left panels of Figures 1-3 are shown in Table 3.

Although the shapes and features of X-ray plateaus are definitely different from those of flares, the above statistical analyses indicate that both X-ray plateaus and flares have similar ratios of energy release from the central engine and similar correlations to the isotropic energy of prompt emission. Thus, we argue that most of X-ray plateaus and flares should have the same physical origin, i.e., a new round of the energy releases from the active central engines, and the different features might be caused by different circumstances and radiation mechanisms.

#### 4. TESTING OF CENTRAL ENGINE MODELS

It is difficult to determine the exact type of central engine based on the GRB observations. Since a stellar-mass BH or an NS should be born in the center of a massive collapsar and compact object merger, the most plausible candidates of the GRB central engine models could be confirmed, i.e., BH hyperaccretion disk and millisecond magnetar. According to the above statistical results, most X-ray plateaus and flares are triggered by central engine activities, so here, we test two popular models to roughly discuss their possible origins and estimate the main influencing factors in the scenarios of BH hyperaccretion and magnetars.

##### 4.1. BH hyperaccretion

Perna et al. (2006) proposed that GRB X-ray flares could be powered by fractured accretion disks. If gravitational instability exists in the accretion disk and the local cooling of the disk is rapid (e.g., Nelson 2000; Liu et

al. 2014), some fragments might be formed in the outer part of the accretion disk. Then, the fragments falling into the BH with a relatively slow in-spiral will lead to large-amplitude changes in the accretion rate; thus, X-ray flares will appear after prompt emission. In this framework, the released energy of each flare is roughly proportional to the mass of each fragment in the outer region of the disk. We consider that this mechanism is also suitable for energy-ejection-driven X-ray plateaus. In the case of the rapid cooling, episodic energy injection can also produce the shapes of plateaus, which has been verified (Huang & Liu 2021); If the slow cooling appears in the disk, it will lead to the redistribution of the disk materials and then maintain a long-lived accretion process (e.g., Liu et al. 2014).

The ratio of the formed fragment (or the extended disk) mass  $M_{\text{frag}}$  to the central BH mass  $M_{\text{BH}}$  can be expressed as (e.g., Takeuchi et al. 1996; Perna et al. 2006)

$$\frac{M_{\text{frag}}}{M_{\text{BH}}} \simeq \left(\frac{H}{R}\right)^2 \alpha^{1/2} \quad (1)$$

where  $H$ ,  $R$ , and  $\alpha$  are the half-thickness of the disk, the distance from the central object to the fragments, and the viscosity parameter, respectively (Shakura & Sunyaev 1973; Kato et al. 2008).

For the extremely geometrically thick disk,  $H \sim R$ , and the typical value of  $M_{\text{BH}}$  is  $\sim 3 M_{\odot}$ . Therefore, we obtain  $M_{\text{frag}} \sim 3\alpha^{1/2} M_{\odot}$ . As the main mechanisms of energy release of GRBs, the neutrino annihilation process (e.g., Liu et al. 2017) and Blandford-Znajek mechanism (Blandford & Znajek 1977; Lee et al. 2000) ask the typical accretion mass  $\sim 3$  and  $1 M_{\odot}$  for the prompt emission of LGRBs, respectively (Liu et al.

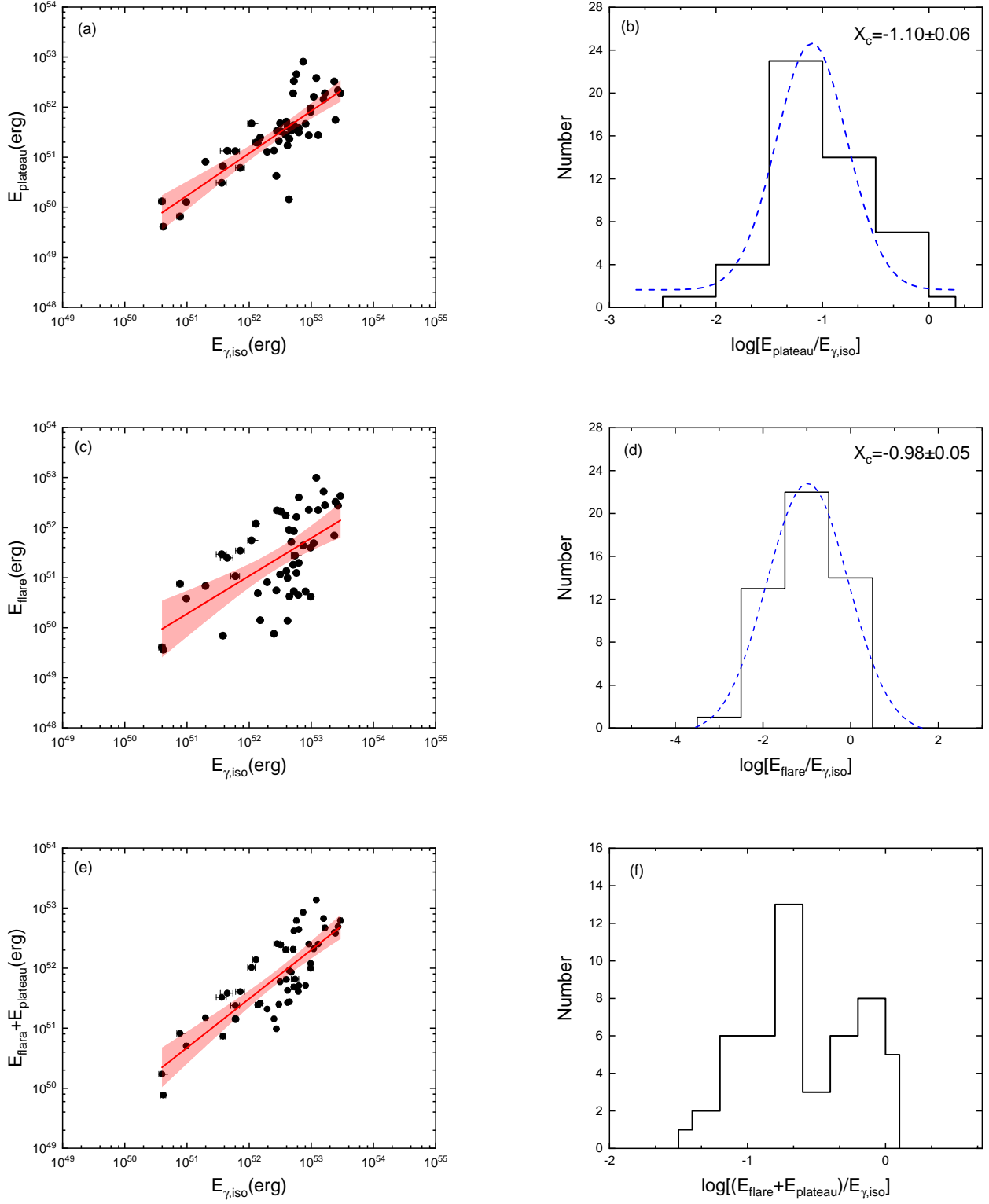


**Figure 3.** *Panels (a, c, e):* Correlations of  $E_{\text{plateau}} - E_{\gamma, \text{iso}}$ ,  $E_{\text{flare}} - E_{\gamma, \text{iso}}$ , and  $(E_{\text{plateau}} + E_{\text{flare}}) - E_{\gamma, \text{iso}}$  for 51 GRBs with both flares and plateaus. The red solid lines correspond to the linear fitting with slopes of  $\sim 0.85 \pm 0.09$ ,  $0.76 \pm 0.14$ , and  $0.82 \pm 0.08$ . *Panels (b, d, f):* Histogram of  $\log(E_{\text{plateau}}/E_{\gamma, \text{iso}})$ ,  $\log(E_{\text{flare}}/E_{\gamma, \text{iso}})$ , and  $\log[(E_{\text{plateau}} + E_{\text{flare}})/E_{\gamma, \text{iso}}]$  for these 51 GRBs. The blue dashed lines are the Gaussian fitting lines with  $X_c = -1.10 \pm 0.06$  and  $-0.98 \pm 0.05$  in *Panels (b)* and *(d)*, respectively.

2015). Considering the above results  $E_{\text{plateau}}/E_{\gamma,\text{iso}}$  (or  $E_{\text{flare}}/E_{\gamma,\text{iso}} \sim 0.1$ , we obtain  $\alpha \sim 0.01$ , which satisfies the requirements on the cooling timescale and gravitational instability (Perna et al. 2006).

#### 4.2. Magnetars

In the magnetar scenario, the energy injection can be driven by the spin-down of magnetars to power X-ray plateaus. The total rotation energy can be given by

$$E_{\text{rot}} = \frac{1}{2} I \Omega_0 \simeq 2 \times 10^{52} M_{\text{NS},1.4} R_{\text{NS},6}^2 P_{0,-3}^{-2} \text{ erg}, \quad (2)$$

where  $I$  is the moment of inertia,  $\Omega_0 = 2\pi/P_0$  is the initial angular frequency, and  $M_{\text{NS},1.4} = M/(1.4 M_{\odot})$ ,  $R_{\text{NS},6} = R_{\text{NS}}/(10^6 \text{ cm})$ , and  $P_{0,-3} = P_0/(10^{-3} \text{ s})$  are the dimensionless NS mass, radius, and rotation period, respectively. The LT relation of X-ray plateaus (e.g., Dainotti et al. 2008) can be explained by the magnetar model (e.g., Rowlinson et al. 2014; Rea et al. 2015; Stratta et al. 2018). Of course the winds driven by the rotations could power the X-ray flares (e.g., Dai et al. 2006; Metzger et al. 2011; Mu et al. 2016).

However, the mechanism of the energy release in the GRB prompt emission phase remains uncertain. Kluźniak & Ruderman (1998), Ruderman et al. (2000), and Dai et al. (2006) pointed out that a newborn NS may be unstable, the core and the exterior have different spin speeds, and differential rotation leads to an internal poloidal magnetic field windup. Then, the produced toroidal fields are so strong that the fields float up and break through the surface. An outburst event caused by the magnetic reconnection occurred next, and the burst energy  $E_b$  of each eruption may be estimated as (e.g., Kluźniak & Ruderman 1998)

$$E_b \simeq 6 \times 10^{51} \frac{V_B}{V_*} \text{ erg}, \quad (3)$$

where  $V_B$  and  $V_*$  are the volume of the toroid and the NS, respectively. For a GRB event, the sum of frequent energy released in the GRB prompt emission phase can exceed  $\sim 10^{53}$  erg (e.g., Kluźniak & Ruderman 1998). Then, the ratio of the total or parts of spin-down energy to the energy of differential rotation is easily taken as  $\sim 0.1$ , which conforms to the statistical results.

In conclusion, the BH hyperaccretion and magnetar models are both suitable to explain the observations of

GRB X-ray plateaus and flares. In other words, the verification of the central engines is practicable on their uniform origins, but there is no evidence to constrain and distinguish these models. Moreover, besides the above mentioned BH or NS related central engines, only in the jet modes, the precessing or off-axis jets launched from the whichever central engines are considered as the possible origins of both X-ray plateaus and flares (e.g., Liu et al. 2010; Huang & Liu 2021).

## 5. SUMMARY

In this paper, two samples, including 174 GRBs with plateau phases and 106 GRBs with X-ray flares, are exhibited, of which 51 GRBs overlap in the two samples. One can note three tightly positive correlations with similar slopes for  $E_{\text{plateau}} - E_{\gamma,\text{iso}}$ ,  $E_{\text{flare}} - E_{\gamma,\text{iso}}$ , and  $(E_{\text{plateau}} + E_{\text{flare}}) - E_{\gamma,\text{iso}}$ . The distributions of  $E_{\text{plateau}}/E_{\gamma,\text{iso}}$  and  $E_{\text{flare}}/E_{\gamma,\text{iso}}$  can be fitted with a Gaussian distribution very well, and their median is approximately  $\sim 0.1$ , especially for the overlapping GRB sample. The  $E_{\text{plateau}} - E_{\gamma,\text{iso}}$  correlation still holds for more cases confirming the result of Dainotti et al. (2011b). We argue that both X-ray plateaus and flares might have the same physical origin, but appear with different features in GRB afterglows. We also discuss the applicabilities of two popular models of GRB central engines, i.e., BHs surrounded by fractured hyperaccretion disks and millisecond magnetars.

The central engine of GRBs is still a mystery, and many models have been proposed in the literature. Depending only on multiband observations, it is difficult to solve this puzzle, but the multimessenger era might offer the possibility via joint detection of electromagnetic radiation, gravitational waves, and MeV neutrinos related to the central engine and progenitors (e.g., Liu et al. 2017).

## ACKNOWLEDGMENTS

We thank Zi-Gao Dai and Shu-Qing Zhong for helpful discussion. This work was supported by the National Natural Science Foundation of China under grants U2038106, 11822304, and 12173031.

## REFERENCES

- Beniamini, P., Duque, R., Daigne, F., et al. 2020, MNRAS, 492, 2847
- Bernardini, M. G., Margutti, R., Chincarini, G., et al. 2011, A&A, 526, A27
- Blandford, R. D. & Znajek, R. L. 1977, MNRAS, 179, 433

- Bucciantini, N., Metzger, B. D., Thompson, T. A., et al. 2012, *MNRAS*, 419, 1537
- Burrows, D. N., Romano, P., Falcone, A., et al. 2005, *Science*, 309, 1833
- Chincarini, G., Mao, J., Margutti, R., et al. 2010, *MNRAS*, 406, 2113
- Dai, Z. G. & Lu, T. 1998a, *A&A*, 333, L87
- Dai, Z. G. & Lu, T. 1998b, *PhRvL*, 81, 4301
- Dai, Z. G., Wang, X. Y., Wu, X. F., et al. 2006, *Science*, 311, 1127
- Dainotti, M. G., Cardone, V. F., & Capozziello, S. 2008, *MNRAS*, 391, L79
- Dainotti, M. G., Cardone, V. F., Piedipalumbo, E., et al. 2013b, *MNRAS*, 436, 82
- Dainotti, M. G. & Del Vecchio, R. 2017, *NewAR*, 77, 23
- Dainotti, M. G., Del Vecchio, R., Shigehiro, N., et al. 2015b, *ApJ*, 800, 31
- Dainotti, M. G., Fabrizio Cardone, V., Capozziello, S., et al. 2011a, *ApJ*, 730, 135
- Dainotti, M. G., Hernandez, X., Postnikov, S., et al. 2017, *ApJ*, 848, 88
- Dainotti, M. G., Livermore, S., Kann, D. A., et al. 2020, *ApJL*, 905, L26
- Dainotti, M. G., Omodei, N., Srinivasaragavan, G. P., et al. 2021, *ApJS*, 255, 13
- Dainotti, M. G., Ostrowski, M., & Willingale, R. 2011b, *MNRAS*, 418, 2202
- Dainotti, M. G., Petrosian, V., Singal, J., et al. 2013a, *ApJ*, 774, 157
- Dainotti, M. G., Petrosian, V., Willingale, R., et al. 2015a, *MNRAS*, 451, 3898
- Dainotti, M. G., Postnikov, S., Hernandez, X., et al. 2016, *ApJL*, 825, L20
- Dainotti, M. G., Willingale, R., Capozziello, S., et al. 2010, *ApJL*, 722, L215
- Du, M., Yi, S.-X., Liu, T., et al. 2021, *ApJ*, 908, 242
- Du, S. 2020, *ApJ*, 901, 75
- Duffell, P. C. & MacFadyen, A. I. 2015, *ApJ*, 806, 205
- Eichler, D., Livio, M., Piran, T., et al. 1989, *Nature*, 340, 126
- Falcone, A. D., Morris, D., Racusin, J., et al. 2007, *ApJ*, 671, 1921
- Fan, Y. & Piran, T. 2006, *MNRAS*, 369, 197
- Fana Dirirsa, F., Razzaque, S., Piron, F., et al. 2019, *ApJ*, 887, 13
- Gehrels, N., Chincarini, G., Giommi, P., et al. 2004, *ApJ*, 611, 1005
- Gompertz, B. P., O'Brien, P. T., Wynn, G. A., et al. 2013, *MNRAS*, 431, 1745
- Hao, J.-M., Cao, L., Lu, Y.-J., et al. 2020, *ApJS*, 248, 21
- Hou, S.-J., Liu, T., Gu, W.-M., et al. 2014, *ApJL*, 781, L19
- Hou, S.-J., Liu, T., Xu, R.-X., et al. 2018, *ApJ*, 854, 104
- Huang, B.-Q. & Liu, T. 2021, *ApJ*, 916, 71
- Ioka, K., Toma, K., Yamazaki, R., et al. 2006, *A&A*, 458, 7
- Kato, S., Fukue, J., & Mineshige, S. 2008, *Black-Hole Accretion Disks: Towards a New Paradigm* (Kyoto, Japan:Kyoto University Press)
- King, A., O'Brien, P. T., Goad, M. R., et al. 2005, *ApJL*, 630, L113
- Kluźniak, W. & Ruderman, M. 1998, *ApJL*, 505, L113
- Lazzati, D., Blackwell, C. H., Morsony, B. J., et al. 2011, *MNRAS*, 411, L16
- Lazzati, D., Perna, R., & Begelman, M. C. 2008, *MNRAS*, 388, L15
- Lee, H. K., Brown, G. E., & Wijers, R. A. M. J. 2000, *ApJ*, 536, 416
- Lee, W. H., Ramirez-Ruiz, E., & López-Cámara, D. 2009, *ApJL*, 699, L93
- Li, A., Zhang, B., Zhang, N.-B., et al. 2016, *PhRvD*, 94, 083010
- Li, Y., Zhang, B., & Lü, H.-J. 2016, *ApJS*, 227, 7
- Liu, T., Gu, W.-M., Xue, L., et al. 2008, *ApJ*, 676, 545
- Liu, T., Gu, W.-M., & Zhang, B. 2017, *NewAR*, 79, 1
- Liu, T., Hou, S.-J., Xue, L., et al. 2015, *ApJS*, 218, 12
- Liu, T., Liang, E.-W., Gu, W.-M., et al. 2010, *A&A*, 516, A16
- Liu, T., Song, C.-Y., Yi, T., et al. 2019, *Journal of High Energy Astrophysics*, 22, 5
- Liu, T., Song, C.-Y., Zhang, B., et al. 2018, *ApJ*, 852, 20
- Liu, T., Yu, X.-F., Gu, W.-M., et al. 2014, *ApJ*, 791, 69
- Luo, Y., Gu, W.-M., Liu, T., et al. 2013, *ApJ*, 773, 142
- MacFadyen, A. I. & Woosley, S. E. 1999, *ApJ*, 524, 262
- Margutti, R., Chincarini, G., Granot, J., et al. 2011, *MNRAS*, 417, 2144.
- Margutti, R., Guidorzi, C., Chincarini, G., et al. 2010, *MNRAS*, 406, 2149.
- Metzger, B. D., Giannios, D., Thompson, T. A., et al. 2011, *MNRAS*, 413, 2031
- Mészáros, P. & Rees, M. J. 1997, *ApJ*, 476, 232
- Minaev, P. Y. & Pozanenko, A. S. 2020, *MNRAS*, 492, 1919
- Mu, H.-J., Gu, W.-M., Hou, S.-J., et al. 2016, *ApJ*, 832, 161
- Mu, H.-J., Gu, W.-M., Mao, J., et al. 2018, *ApJ*, 858, 34
- Narayan, R., Piran, T., & Kumar, P. 2001, *ApJ*, 557, 949
- Narayan, R., Paczyński, B., & Piran, T. 1992, *ApJL*, 395, L83
- Nelson, C. H. 2000, *ApJL*, 544, L91
- Nousek, J. A., Kouveliotou, C., Grupe, D., et al. 2006, *ApJ*, 642, 389
- Ouyed, R., Leahy, D., & Koning, N. 2020, *Research in Astronomy and Astrophysics*, 20, 027

- O'Brien, P. T. & Willingale, R. 2007, *Philosophical Transactions of the Royal Society of London Series A*, 365, 1179
- Panaiteacu, A., Mészáros, P., Burrows, D., et al. 2006, *MNRAS*, 369, 2059
- Panaiteacu, A., Mészáros, P., & Rees, M. J. 1998, *ApJ*, 503, 314
- Paczyński, B. 1986, *ApJL*, 308, L43
- Perna, R., Armitage, P. J., & Zhang, B. 2006, *ApJL*, 636, L29
- Popham, R., Woosley, S. E., & Fryer, C. 1999, *ApJ*, 518, 356
- Proga, D. & Zhang, B. 2006, *MNRAS*, 370, L61
- Rea, N., Gullón, M., Pons, J. A., et al. 2015, *ApJ*, 813, 92
- Rees, M. J. & Mészáros, P. 1992, *MNRAS*, 258, 41
- Rowlinson, A., Gompertz, B. P., Dainotti, M., et al. 2014, *MNRAS*, 443, 1779
- Rowlinson, A., O'Brien, P. T., Tanvir, N. R., et al. 2010, *MNRAS*, 409, 531
- Ruderman, M. A., Tao, L., & Kluźniak, W. 2000, *ApJ*, 542, 243
- Ruffini, R., Wang, Y., Aimuratov, Y., et al. 2018, *ApJ*, 852, 53
- Sakamoto, T., Hill, J. E., Yamazaki, R., et al. 2007, *ApJ*, 669, 1115
- Shakura, N. I. & Sunyaev, R. A. 1973, *A&A*, 500, 33
- Sari, R., Piran, T., & Narayan, R. 1998, *ApJL*, 497, L17
- Si, S.-K., Qi, Y.-Q., Xue, F.-X., et al. 2018, *ApJ*, 863, 50
- Stratta, G., Dainotti, M. G., Dall'Osso, S., et al. 2018, *ApJ*, 869, 155
- Takeuchi, T., Miyama, S. M., & Lin, D. N. C. 1996, *ApJ*, 460, 832
- Tang, C.-H., Huang, Y.-F., Geng, J.-J., et al. 2019, *ApJS*, 245, 1
- Toma, K., Ioka, K., Yamazaki, R., et al. 2006, *ApJL*, 640, L139
- Uhm, Z. L. & Beloborodov, A. M. 2007, *ApJL*, 665, L93
- Usov, V. V. 1992, *Nature*, 357, 472
- Wang, F.-F., Zou, Y.-C., Liu, Y., et al. 2018, *Journal of High Energy Astrophysics*, 18, 21
- Woosley, S. E. 1993, *ApJ*, 405, 273
- Yamazaki, R. 2009, *ApJL*, 690, L118
- Yi, S.-X., Lei, W.-H., Zhang, B., et al. 2017, *Journal of High Energy Astrophysics*, 13, 1
- Yi, S.-X., Xi, S.-Q., Yu, H., et al. 2016, *ApJS*, 224, 20
- Yi, S.-X., Wu, X.-F., Wang, F.-Y., et al. 2015, *ApJ*, 807, 92
- Yi, S.-X., Wu, X.-F., & Dai, Z.-G. 2013, *ApJ*, 776, 120
- Yi, S.-X., Wu, X.-F., Zou, Y.-C., et al. 2020, *ApJ*, 895, 94
- Yuan, F. & Zhang, B. 2012, *ApJ*, 757, 56
- Zhang, B., Fan, Y. Z., Dyks, J., et al. 2006, *ApJ*, 642, 354
- Zhang, B. & Mészáros, P. 2001, *ApJL*, 552, L35
- Zhang, B.-B., Zhang, B., Murase, K., et al. 2014, *ApJ*, 787, 66
- Zhou, Q.-Q., Yi, S.-X., Huang, X.-L., et al. 2020, *International Journal of Modern Physics D*, 29, 2050043
- Zou, Y. C., Wu, X. F., & Dai, Z. G. 2005, *MNRAS*, 363, 93



**Table 1.** Data of GRBs with X-ray plateaus.

GRB	$z$	$E_{\gamma, \text{iso}}$ ( $10^{51}$ erg)	$E_{\text{plateau}}$ ( $10^{50}$ erg)	GRB	$z$	$E_{\gamma, \text{iso}}$ ( $10^{51}$ erg)	$E_{\text{plateau}}$ ( $10^{50}$ erg)
050315	1.949	30.200±1.391	51.248	050319	3.24	29.512±3.398	1.983
050401	2.9	154.882±7.133	151.728	<b>050416A</b>	0.6535	0.417±0.038	0.406
050505	4.27	87.096±6.016	240.885	<b>050730</b>	3.97	74.131±5.121	806.04
050801	1.38	1.549±0.214	1.401	<b>050802</b>	1.71	15.136±1.046	24.715
<b>050803</b>	0.422	0.977±0.068	1.267	<b>050814</b>	5.3	97.724±11.251	95.354
050824	0.83	0.490±0.090	1.487	050922C	2.199	19.055±0.439	35.076
<b>051016B</b>	0.9364	0.398±0.046	1.309	051109A	2.346	28.840±3.320	66.761
051109B	0.08	0.004±0.001	0.001	051221A	0.547	0.912±0.021	0.331
<b>060108</b>	2.03	3.802±0.350	6.629	<b>060115</b>	3.53	44.668±4.114	23.233
060116	4	75.858±6.987	17.337	060202	0.78	3.467±0.240	1.176
060206	4.05	26.915±1.240	66.572	<b>060210</b>	3.91	234.423±10.796	324.4
060502A	1.51	13.804±0.636	8.311	<b>060522</b>	5.11	52.481±4.834	43.255
<b>060526</b>	3.21	28.184±3.245	33.441	<b>060604</b>	2.1357	4.467±1.029	13.376
060605	3.8	20.417±2.351	76.075	<b>060607A</b>	3.082	52.481±2.417	331.797
060614	0.13	0.813±0.019	0.09	<b>060707</b>	3.43	39.811±3.667	50.863
060708	2.3	6.310±0.436	15.435	<b>060714</b>	2.71	47.863±2.204	33.836
<b>060729</b>	0.54	1.995±0.138	8.082	<b>060814</b>	0.84	27.542±0.634	4.215
<b>060906</b>	3.685	61.660±4.259	36.367	<b>060908</b>	1.8836	25.119±1.157	13.488
060912A	0.937	3.162±0.146	0.599	061021	0.3463	0.891±0.021	0.416
<b>061121</b>	1.314	63.096±1.453	31.215	061201	0.111	0.010±0.001	0.018
061222A	2.088	85.114±1.960	99.926	070110	2.352	21.380±1.477	118.933
<b>070129</b>	2.3384	38.905±3.583	27.768	070208	1.165	1.622±0.336	2.215
<b>070306</b>	1.497	31.623±1.456	47.579	070506	2.31	2.692±0.310	6.307
070508	0.82	35.481±0.817	13.492	070529	2.4996	38.019±3.502	13.932
070714B	0.92	1.622±0.187	1.055	<b>070721B</b>	3.626	97.724±4.500	80.391
070809	0.22	0.012±0.001	0.019	070810A	2.17	7.943±0.732	9.573
071020	2.145	25.704±1.184	38.692	<b>080310</b>	2.43	32.359±2.980	32.756
080430	0.767	1.905±0.132	1.85	080516	3.2	5.754±0.795	24.731
080603B	2.69	39.811±1.833	53.337	080605	1.6398	91.201±2.100	52.671
080707	1.23	2.089±0.241	1.855	080721	2.602	186.209±12.863	611.707
<b>080810</b>	3.35	109.648±5.049	161.618	080905B	2.374	23.988±2.762	88.745
081007	0.5295	0.525±0.060	0.462	<b>081008</b>	1.9685	41.687±1.920	17.082
081029	3.8479	61.660±5.679	96.728	081221	2.26	223.872±5.155	152.482
090113	1.7493	5.888±0.271	10.696	090205	4.7	7.586±1.048	39.434
090313	3.375	33.884±4.681	144.87	<b>090407</b>	1.4485	6.026±0.971	13.149
090418A	1.608	30.903±1.423	27.945	<b>090423</b>	8	51.286±3.543	188.037
090510	0.903	0.741±0.085	2.135	<b>090516</b>	4.109	295.121±20.386	189.817
090519	3.9	36.308±2.508	3.717	090529	2.625	10.715±2.467	13.162
090530	1.266	4.677±0.431	1.974	090618	0.54	79.433	7.718
090927	1.37	1.000±0.138	3.053	091018	0.971	3.548±0.245	4.024
<b>091029</b>	2.752	41.687±1.920	41.14	091109A	3.5	40.738±4.690	8.979
091127	0.49	5.623±0.129	9.62	091208B	1.0633	10.000±0.691	3.123
100219A	4.7	14.791±2.384	73.43	<b>100302A</b>	4.813	12.882±1.483	19.697
100418A	0.6235	0.347±0.048	1.149	100424A	2.465	21.380±1.477	93.262
100425A	1.755	3.715±0.684	2.819	<b>100513A</b>	4.772	57.544±3.975	35.59
100615A	1.398	25.704±0.592	41.672	100621A	0.542	16.218	3.374
<b>100704A</b>	3.6	158.489±3.649	142.154	100814A	1.44	48.978±1.128	57.199

<b>100901A</b>	1.408	10.965±1.515	46.952	<b>100902A</b>	4.5	120.226±8.305	380.507
<b>100906A</b>	1.727	91.201	27.27	101219B	0.5519	1.698±0.313	0.214
110213A	1.46	33.113±2.287	66.212	110715A	0.82	21.380±0.492	5.496
110808A	1.348	1.585±0.328	2.295	111008A	5	234.423±10.796	322.219
111123A	3.1516	158.489±7.299	67.331	<b>111209A</b>	0.677	43.652±1.005	1.427
111228A	0.71627	11.749±0.271	4.023	111229A	1.3805	1.698±0.313	6.407
120118B	2.943	34.674±1.597	26.658	120326A	1.798	21.380±2.461	92.65
120327A	2.813	64.565±1.487	43.779	120404A	2.876	29.512±2.039	28.733
120422A	0.28	0.045±0.007	0.052	120521C	6	63.096±5.811	46.249
120712A	4.1745	60.256±2.775	65.143	<b>120802A</b>	3.796	54.954±7.592	38.096
120811C	2.671	48.978±4.511	38.44	120922A	3.1	128.825±14.832	43.932
<b>121024A</b>	2.298	13.804±1.271	19.42	<b>121128A</b>	2.2	81.283±3.743	46.254
<b>121211A</b>	1.023	3.631±0.669	3.062	130131B	2.539	5.129±0.590	10.444
130408A	3.758	66.069±10.649	108.999	130420A	1.297	31.623±1.456	4.377
130511A	1.3033	1.000±0.161	1.181	<b>130514A</b>	3.6	245.471±5.652	55.304
130603B	0.3564	0.204±0.009	0.277	<b>130606A</b>	5.913	165.959±11.464	190.4
130612A	2.006	2.291±0.475	2.333	<b>131030A</b>	1.293	128.825	27.568
<b>131103A</b>	0.599	0.776±0.089	0.651	131105A	1.686	51.286±3.543	19.912
<b>140114A</b>	3	63.096±1.453	38.2	<b>140206A</b>	2.73	269.153±6.197	214.639
140213A	1.2076	46.774	27.792	<b>140304A</b>	5.283	57.544±3.975	455.163
<b>140430A</b>	1.6	7.244±1.168	6.095	<b>140512A</b>	0.725	19.498±0.449	12.788
140518A	4.707	40.738±3.752	58.399	140614A	4.233	44.668±12.342	35.379
140629A	2.275	30.200±2.086	28.524	140703A	3.14	83.176±5.746	153.816
140903A	0.351	0.044±0.003	0.252	141004A	0.57	0.575±0.027	0.286
141026A	3.35	30.903±2.135	44.513	<b>141121A</b>	1.47	30.200±2.086	21.023
150323A	0.539	5.623±0.129	0.378	150403A	2.06	177.828±4.095	452.607
150423A	1.394	0.324±0.045	0.456	150424A	3	29.512±2.039	30.343
150910A	1.359	23.442±1.619	62.048	151027A	0.81	13.804±0.318	30.039
151027B	4.063	47.863±8.817	58.131	151112A	4.1	30.903±3.558	104.129
151215A	2.59	4.786±0.992	9.663	160121A	1.96	5.888±0.407	13.53
160227A	2.38	41.687±2.880	67.44	160303A	2.3	1.905±0.351	2.446
160314A	0.726	0.398±0.055	0.585	160327A	4.99	61.660±4.259	84.611
160804A	0.736	16.596±0.382	0.89	161108A	1.159	3.981±0.367	3.501
161117A	1.549	125.893	18.466	170113A	1.968	6.457±0.595	29.68
170202A	3.65	89.125±2.052	70.381	170519A	0.818	1.995±0.322	2.568
170607A	0.557	6.166±0.284	1.916	170705A	2.01	95.499±2.199	86.809
170714A	0.793	4.677±0.431	129.891	171205A	0.0368	0.011±0.001	0.003
171222A	2.409	26.303±2.423	19.17	180115A	2.487	10.965±1.515	16.69
180325A	2.25	79.433±1.829	135.483	180329B	1.998	32.359±2.980	14.349
180404A	1	3.467±0.240	1.262	180720B	0.654	97.724±2.250	73.881

**Table 2.** Data of GRBs with X-ray flares.

GRB	$z$	$E_{\gamma,\text{iso}}$ ( $10^{51}$ erg)	$E_{\text{flare}}$ ( $10^{50}$ erg)	GRB	$z$	$E_{\gamma,\text{iso}}$ ( $10^{51}$ erg)	$E_{\text{flare}}$ ( $10^{50}$ erg)
050714B	2.4383	49.900	0.556	050406	2.44	2.300±0.800	1.740
<b>050416A</b>	0.65	0.617	0.363	050502B	5.2	26.600	41.466
050607	4	123.000	2.869	050724	0.257	0.090±0.020	0.210
<b>050730</b>	3.97	74.131±5.121	43.620	<b>050802</b>	1.71	56.600	1.411
<b>050803</b>	0.422	0.977±0.068	3.800	<b>050814</b>	5.3	99.000	4.143
050819	2.5043	102.000	0.402	050820A	2.612	1033.600±36.000	482.000
050822	1.43	25.500	0.420	050904	6.1	1333.6±138.9	370.800
050908	3.35	19.700±3.200	3.360	050915A	2.5273	18.0±13	2.960
050922B	4.5	67.610	13.246	051006	1.059	4.898	0.159
<b>051016B</b>	0.94	0.370	0.404	051227	0.714	1.200	0.026
<b>060108</b>	2.03	5.900	0.692	060111A	2.32	14.790	13.048
<b>060115</b>	3.53	44.668±4.114	4.200	060124	2.3	437.9±63.9	554.900
<b>060210</b>	3.91	234.423±10.796	69.000	060223A	4.41	97.3±7.2	7.500
060418	1.49	135.5±27.1	20.100	060510B	4.9	367.000±28.700	290.800
060512	0.4428	0.325	0.090	<b>060522</b>	5.11	52.481±4.834	5.320
<b>060526</b>	3.21	28.184±3.245	221.110	<b>060604</b>	2.1357	4.467±1.029	24.830
<b>060607A</b>	3.082	52.481±2.417	84.890	<b>060707</b>	3.43	39.811±3.667	13.560
<b>060714</b>	2.71	47.863±2.204	51.330	060719	1.532	14.000±1.300	0.340
<b>060729</b>	0.54	16.000	6.783	<b>060814</b>	0.84	138.040	5.563
060904B	0.703	3.640±0.740	15.900	<b>060906</b>	3.69	52.480	4.471
<b>060908</b>	1.8836	72.000	0.757	060926	3.208	11.500	5.800
<b>061121</b>	1.314	63.096±1.453	19.700	070103	2.6208	10.900	0.560
<b>070129</b>	2.3384	38.905±3.583	175.110	<b>070306</b>	1.4959	82.600	11.566
070318	0.836	9±2	1.460	<b>070721B</b>	3.626	97.724±4.500	39.740
070724A	0.457	0.016±0.003	0.290	071021	2.452	81.800±8.200	22.820
071031	2.692	39±6	167.800	071112C	0.823	11.800±1.900	0.720
071122	1.14	4.620	0.130	080210	2.641	51.3±2.13	9.110
<b>080310</b>	2.4266	32.359±2.980	212.600	080607	3.036	2171.000±60.000	120.000
080805	1.505	71.600±19.000	10.600	<b>080810</b>	3.35	109.648±5.049	48.800
080906	2	212.000±12.000	36.050	080913	6.44	86.000±25.000	63.090
080928	1.692	28.2±11.7	70.540	<b>081008</b>	1.9685	41.687±1.920	9.780
<b>090407</b>	1.4485	6.026±0.971	10.700	090417B	0.35	1.570	4.159
<b>090423</b>	8	51.286±3.543	18.100	<b>090516</b>	3.9	295.121±20.386	428.340
090715B	3	205.000±19.000	246.980	090809	2.737	18.800±2.600	58.310
090812	2.452	271.800±9.700	49.700	<b>091029</b>	2.752	41.687±1.920	1.380
<b>100302A</b>	4.813	12.882±1.483	118.750	<b>100513A</b>	4.772	57.544±3.975	12.400
<b>100704A</b>	3.6	158.489±3.649	525.100	100728A	1.567	1140.000±68.000	167.800
100816A	0.8034	73.000±0.200	1.680	<b>100901A</b>	1.408	10.965±1.515	55.850
<b>100902A</b>	4.5	120.226±8.305	985.000	<b>100906A</b>	1.727	91.201	225.000
110205A	1.98	483.000±64.000	159.610	110801A	1.858	109.000±27.000	99.340
111107A	2.893	37.600±5.500	2.610	<b>111209A</b>	0.677	43.652±1.005	90.190
<b>120802A</b>	3.796	54.954±7.592	27.500	<b>121024A</b>	2.298	13.804±1.271	4.870
<b>121128A</b>	2.2	81.283±3.743	5.290	<b>121211A</b>	1.023	3.631±0.669	29.400
121229A	2.707	37.000±11.000	36.200	130427B	2.78	31.6±17.5	4.360
<b>130514A</b>	3.6	245.471±5.652	325.200	<b>130606A</b>	5.91	165.959±11.464	277.800
130925A	0.347	150.000±3.000	17.770	131004A	0.717	0.690±0.030	0.110
<b>131030A</b>	1.293	128.825	224.000	<b>131103A</b>	0.599	0.776±0.089	7.510

131117A	4.042	10.300±1.800	6.190	<b>140114A</b>	3	63.096±1.453	402.100
<b>140206A</b>	2.73	269.153±6.197	275.000	140301A	1.416	9.500±1.800	1.390
<b>140304A</b>	5.283	57.544±3.975	161.900	<b>140430A</b>	1.6	7.244±1.168	34.470
140506A	0.889	14.000±1.400	67.330	<b>140512A</b>	0.725	19.498±0.449	8.040
140515A	6.32	53.800±5.800	56.300	140710A	0.558	0.257	0.150
<b>141221A</b>	1.452	24.600±0.350	3.850	150206A	2.087	619.000±45.000	346.000

---

**Table 3.** Results of the linear regression analyses for GRB samples.

Correlations	Slope	Intercept	Pearson's $r$
$(E_{\text{plateau}} - E_{\gamma,\text{iso}})^{\dagger}$	$0.95 \pm 0.04$	$1.40 \pm 1.96$	0.89
$(E_{\text{flare}} - E_{\gamma,\text{iso}})^{\ddagger}$	$0.80 \pm 0.09$	$9.22 \pm 4.50$	0.67
$(E_{\text{plateau}} - E_{\gamma,\text{iso}})^{\S}$	$0.85 \pm 0.09$	$7.01 \pm 4.58$	0.81
$(E_{\text{flare}} - E_{\gamma,\text{iso}})^{\S}$	$0.76 \pm 0.14$	$11.70 \pm 7.43$	0.61
$[(E_{\text{plateau}} + E_{\text{flare}}) - E_{\gamma,\text{iso}}]^{\S}$	$0.82 \pm 0.08$	$9.08 \pm 4.32$	0.82

$\dagger$  The plateau sample.

$\ddagger$  The flare sample.

$\S$  The overlapping sample.